# MAGNETIC IRON OXIDES NANOPARTICLES OBTAINED BY MECHANOCHEMICAL REACTIONS FROM DIFFERENT SOLID PRECURSORS

Pedro A. Calderón Bedoya[1], Pablo M. Botta[1*], Paula G. Bercoff[2], María A. Fanovich[1]

[1] Instituto de Investigaciones en Ciencia y Tecnología de Materiales, INTEMA (UNMdP-CONICET), Av. Colón 10850, 7600 Mar del Plata, Argentina.

[2] Facultad de Matemática, Astronomía, Física y Computación, FAMAF (UNC), Instituto de Física Enrique Gaviola, IFEG (UNC-CONICET), Medina Allende s/n, Ciudad Universitaria, Córdoba, Argentina.

* Corresponding author

## ABSTRACT

In this study, iron oxide nanoparticles (NPs) were successfully prepared from three different reactive systems by using mechanochemical synthesis. The effect of using iron salts with different oxidation state and the addition of metallic Fe to the mixture reactive was investigated. The influence of different mechanochemical treatments times on the structural and magnetic properties of the obtained iron oxide NPs was also studied. Composition, crystal structure and morphology of the nanoparticles were analyzed by XRD, Raman spectroscopy, SEM, TEM and DLS techniques. The obtained crystalline NPs exhibited mean sizes of about 8-10 nm and agglomerate in clusters of about 300 nm. Also, magnetic properties as a function of temperature and applied field were determined for the obtained iron oxide NPs, showing high magnetization in the whole temperature range. The results indicated that the presence of metallic Fe in the starting mixture plays a crucial role in the formation of spinel magnetic phases (magnetite/maghemite). Structural and magnetic results are consistent with the formation of maghemite in the studied samples.

## INTRODUCTION

Spinel ferrites are crystalline iron oxides whose magnetic properties have been recognized for their commercial importance since the early 1900's. Magnetite, one of the best-known members of this family, is the first magnetic material discovered by man [1]. Spinel ferrites have the general formula $MFe_2O_4$, where M is a divalent metal such as manganese, nickel, iron, cobalt or magnesium [2]. These oxides crystallize in a cubic system, space group Fd-3m, where the oxygen ions are arranged in a cubic close-packed (fcc) structure and the metal cations occupy the tetrahedral and octahedral interstitials. Because of their high Neél's temperatures, spinels exhibit a ferrimagnetic response at room temperature, typically showing magnetic loops with high saturation magnetization (Ms) values and low coercive fields (Hc) [3,4]. However, when the particle size is below a critical size ─usually a few nanometers─, the magnetic behavior of these ferrites is described as superparamagnetic, which refers to extremely large magnetic moments, produced because of competition between anisotropy and thermal energies [5]. This property of ferrites has been exploited for several applications, such as separation of bio molecules, targeted delivery of drugs, proteins, antibodies and nucleic acids, hyperthermia, biosensing, etc.[6-7]. Because it is known that proton relaxation times are altered in the presence of induced local magnetic moments, it has recently been proposed that ferrite nanoparticles (NPs) can be used for diagnostic purposes in magnetic resonance imaging (MRI), for visualizing tumors and metastases in liver, spleen and lymph nodes, for angiography as a blood pool agent and for visualizing inflammatory lesions like atherosclerotic plaques [8]. The utility of these NPs in biomedical fields is successful not only because of the inherent magnetic properties, but also from the tailored features such as crystal structure, size, and shape [9-10].

Among the different types of iron oxide NPs, magnetite ($Fe_3O_4$), maghemite ($\gamma$-$Fe_2O_3$) and mixed ferrites ($MFe_2O_4$ where M = Co, Mn, Ni or Zn) are the most frequently studied. Different methods have been reported to synthesize iron oxide NPs, such as microwave and ultrasonication assisted syntheses, coprecipitation, chemical reduction, hydrothermal methods, bio-mediated synthesis, and others [11-16]. Among those methods, mechanochemical synthesis is an economic and relatively fast method, which does not generate toxic residues and allows to obtain NPs of controlled size. Also, for biomedical applications this preparative route offers the possibility to increase the production scale [17]. An interesting alternative mechanochemical technique for the synthesis of metallic and oxides NPs, including $TiO_2$, ZnO and $Fe_2O_3$, has been developed by McCormick *et al.* [18-20]. In this method, an acid metallic salt is mechanically treated together with a base (NaOH, $Na_2CO_3$, etc.) producing small crystals of the metallic oxide and a soluble salt as a byproduct. By means of a simple washing operation, the salt can be easily removed, obtaining pure oxide NPs [21,22].

Mechanochemical synthesis of iron oxide NPs has shown to be effective in the evolution of pure phases. This preparative route is an interesting method because it allows to obtain relatively large amounts of material at ambient conditions without using organic reagents. Moreover, the generation of punctual defects and new surfaces in the treated solids can modify the cation distribution within the lattice, with the possibility of improving the magnetic properties, which are highly dependent on the milling conditions (time, mass ratio, atmosphere, milling materials, etc.) [23].

Recently, Medina *et al.* [24] observed the formation of $Fe_3O_4$ by milling mixtures of ferric salts and $NaBH_4$, without using solvents. The obtained $Fe_3O_4$ NPs were relatively stable under water suspension and air exposure, with an average size of 60 nm. However, the authors have not measured magnetization values, describing only qualitatively the observed magnetic properties. Park *et al.* reported the preparation of well-dispersed $Fe_3O_4$ NPs (with sizes around 10–20 nm) produced by mechanochemical transformation of iron oxyhydroxides (FeO(OH)) with good properties to be applied as anodes for rechargeable Li-ion batteries [25]. Iwasaki *et al*. [26-27] investigated a mechanochemical process where a suspension of ferric hydroxide precursor was milled at room temperature using a horizontal tumbling ball mill (stainless-steel reactor and balls). They found that ferric hydroxide was transformed to magnetite without using a reducing reactive. Single-phase magnetite was obtained after 16 h of milling, because of oxidation–reduction reactions between ferric hydroxide and metallic iron coming from the milling vials and balls. This uncontrolled reactivity is questionable and possibly irreproducible at large scale. Carvalho *et al.* reported the preparation of magnetite NPs (12-20 nm) by high energy ball milling, from stoichiometric amounts of distilled water and metallic iron powder. However, the method required long treatment times and the obtained material contained 14% metallic iron as secondary phase [28].

In this context, the aim of this work is to synthesize iron oxide NPs by mechanochemical process using a high-energy planetary ball mill, trying to overcome the previously described drawbacks. Three different solid starting mixtures are used, where the influence of added Fe powder as reactant is comparatively analyzed. Also, the effect of the mechanochemical treatment time on the properties of the obtained iron oxide NPs is investigated. A discussion related to the nature of the reactive system, particle size and magnetic properties of the iron oxide NPs is presented.

## MATERIALS AND METHODS

Ferric chloride hexahydrate ($FeCl_3.6H_2O$, Biopack), ferrous chloride tetrahydrate ($FeCl_2.4H_2O$, Sigma-Aldrich), Fe powder (Carlo Erba) and sodium hydroxide (NaOH, Anedra) were used as precursors for the synthesis of IONPs. All used chemicals in the experiments were reagents of analytical grade and were used without further purification. Three precursor systems were prepared (10 g per batch), by mixing solid reactants according to the molar ratio of the following magnetite/maghemite formation reactions:

System M1: $$2\ FeCl_3.6H_2O + 6\ NaOH \rightarrow \gamma\text{-}Fe_2O_3 + 6NaCl + 15H_2O \quad (1)$$

System M2: $$FeCl_2.4H_2O + 2\ FeCl_3.6H_2O + 8\ NaOH \rightarrow Fe_3O_4 + 8NaCl + 20\ H_2O \quad (2)$$

System M3: $$8FeCl_3.6H_2O + Fe + 24\ NaOH \rightarrow 3Fe_3O_4 + 24\ NaCl + 60\ H_2O \quad (3)$$

Figure 1 shows the experimental procedures followed to prepare each system and Table 1 summarizes the selected nomenclature according to the $Fe^{3+}$, $Fe^{2+}$, $Fe^o$, NaOH molar ratio used, and the time of mechanochemical (MC) treatment. Each mixture was mechanochemically treated using a planetary high-energy ball mill (Fritsch Pulverisette 7), with stainless-steel balls (diameter 10 mm) and 25 mL vials. The vials were rotated at 1400 rpm during measured times between 2 and 24 h. MC treatments were performed at room temperature and air atmosphere using a ball-to-powder mass ratio of 6.4. After each MC-treatment, the samples were washed with distilled water to eliminate the NaCl byproduct; after that, all the samples were dried for 24 h at 50°C, yielding about 3.5 g of IONPs per batch. These powders were characterized according to the techniques described below.

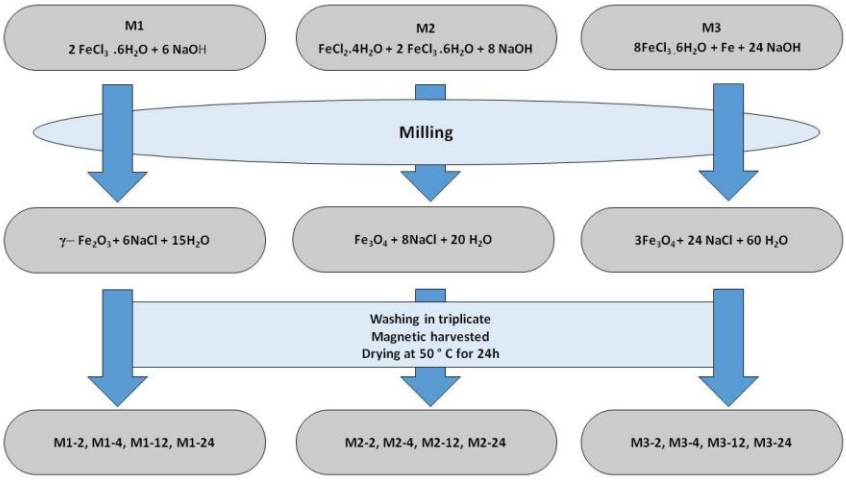


**Figure 1:** Flow chart of the synthesis of iron oxide NPs starting from three different reaction mixtures.

**Table 1:** Precursors, composition and MC-treatment time used for each reaction mixture (M1, M2 and M3).

| System | Precursors (Molar ratio) | | | | Treatment time (h) | Sample |
|---|---|---|---|---|---|---|
| | $FeCl_3.6H_2O$ | $FeCl_2.4H_2O$ | Fe | NaOH | | |
| **M1** | 1 | 0 | 0 | 3 | 2 | M1-2 |
| | | | | | 4 | M1-4 |
| | | | | | 12 | M1-12 |
| | | | | | 24 | M1-24 |
| **M2** | 2 | 1 | 0 | 8 | 2 | M2-2 |
| | | | | | 4 | M2-4 |
| | | | | | 12 | M2-12 |
| | | | | | 24 | M2-24 |
| **M3** | 8 | 0 | 1 | 24 | 2 | M3-2 |
| | | | | | 4 | M3-4 |
| | | | | | 12 | M3-12 |
| | | | | | 24 | M3-24 |

Identification of the crystalline phases was carried out by X-ray diffraction (XRD) in a PANalytical diffractometer with Cu-Kα radiation (wavelength: λ= 1.54050 Å) at 40 kV and 30 mA. Diffractograms were recorded in a 2θ range between 20º and 70º at a scan rate of 1 º/min. The mean crystallite size was estimated from the XRD line broadening measurement, using the Scherrer equation [29] for the main peaks, considering the instrument line width. Lattice parameters (*a*) were calculated according to the following equation for cubic systems, averaging interplanar distances (*d*) corresponding to planes (*h k l)* = (2 2 0), (3 1 1) and (4 4 0):

$$\frac{1}{d^2} = \frac{h^2+k^2+l^2}{a^2} \qquad (4)$$

Raman micro analyses of the obtained powders were performed in a multichannel Renishaw In Via Reflex microspectrometer. Excitation was provided by the 785 nm line of an Ar laser. To enhance the signal-to-noise ratio, 30-50 scans were accumulated, each one having a 15 s exposure to laser power ranging between 30 and 300 mW.

The particle size distributions were determined by dynamic light scattering (DLS) in powder samples with a Malvern Zetasizer nano S90 with a 532 nm laser. Powders were dispersed in distilled water (5 µg in 10 mL) and sonicated for 10 min before each measurement.

Microstructural analysis of the powders was performed by means of scanning electron microscopy (SEM) in a Jeol JXA-8600 instrument. For this purpose, drops of powder dispersions in isopropanol were deposited on glass slides. After solvent evaporation, the samples were coated with a thin gold layer and examined at different magnifications.

Transmission electron microscopy (TEM) images of the particles were obtained in a JEOL (JEM-2100) microscope with a voltage of 120 kV. Prior to observation, the samples were suspended in Cu grids after sonicating an isopropanol suspension of the NPs for several minutes. Particle size distributions were obtained from TEM images, counting a number of elements greater than 200 with the Image Pro Plus software.

Magnetization (M) as a function of magnetic field (H) was measured in a vibrating sample magnetometer Lakeshore 7300. Hysteresis loops were registered at room temperature applying magnetic fields between of -20 and +20 kOe. Before performing the measurements, the powders were compacted in pellets 5 mm in diameter. M(T) curves in zero field cooling/field cooling protocols and M(H) loops at several temperatures in the range from 5 K to 300 K were measured for selected samples in a S700X-R Cryogenic magnetometer.

## RESULTS AND DISCUSSION

The mechanochemical synthesis can be interpreted as proceeding through two physicochemical processes that cannot be separated, namely the production of textural changes which can be detected by microscopy examination, and the alteration of the chemical-structural properties of the material [30-31].

Figure 2 shows XRD patterns of the samples obtained from each reactive mixture (M1, M2 and M3) after MC-treatment for 2, 4, 12 and 24 h, then washed and dried. For samples of the series M1, the absence of peaks corresponding to the reactants confirms the completion of reaction (1), from 2 h of milling. Peaks belonging to the spinel structure (space group Fd-3m) compatible with magnetite ($Fe_3O_4$) or maghemite ($\gamma$-$Fe_2O_3$) are observed. The three most intense peaks appear at about 30.3, 35.5 and 62.9 º2θ (all of which are marked in Figure 2).

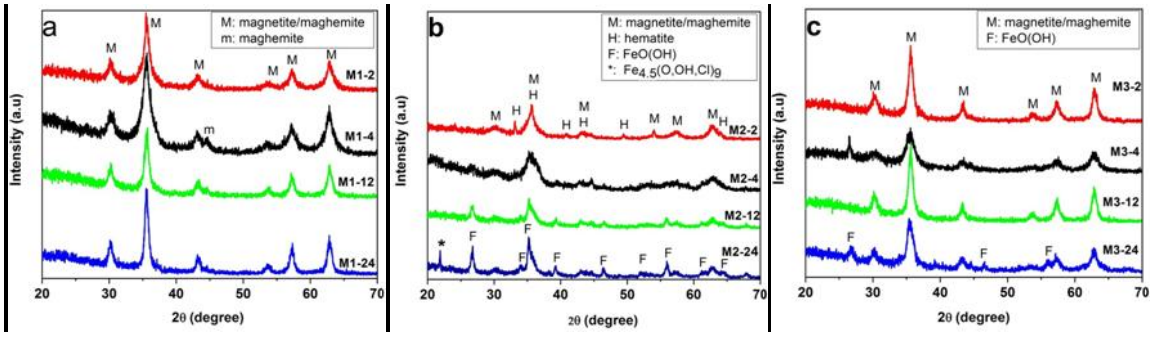


**Figure 2:** XRD patterns of iron oxide NPs after different MC-treatment times for the reactive mixtures **a)** M1, **b)** M2 and **c)** M3. The identified phases are indicated in each graph.

The lattice parameters of these two iron oxides are similar: 0.83960 nm and 0.83515 nm for magnetite (PDF 19-0629) and maghemite (PDF 39-1346) respectively, giving rise to almost identical XRD patterns. This structural similarity and the wide peaks obtained (because of the formation of small crystallites during the mechanochemical reaction) make it difficult to unambiguously assign the XRD peaks in M1-2 either to magnetite or to maghemite. Additional small peaks can be noticed for longer milling times (particularly visible in samples M1-4 and M1-12) which can be related to maghemite. The diffractograms of samples M2 (Figure 2b) show significant differences of reactivity with respect to M1. After two hours of MC-treatment, formation of the spinel structure (magnetite/maghemite) can be observed in sample M2-2. As the milling time increases, the system evolves towards the formation of FeOOH (PDF 81-0464) according to the XRD diagrams of samples M2-12 and M2-24. The detected products in system M2 evidence a low stability of the spinel structure formed after 2 h of milling. The FeOOH phase showed poor conversion to spinel structure because the appropriate conditions for the transformation were not reached in this experimental procedure, compared with the mechanochemical transformation reaction reported by Park *et.al.* [25] where the reactivity of FeOOH to generate $Fe_3O_4$ was facilitated by high temperature (>200°C) and high pressure (6 GPa). Moreover, additional small peaks in the XRD pattern of M2-24 can be assigned to the phase $Fe_{4.5}(O, OH, Cl)_9$. For this reason, in what follows samples coming from mixture M2 will not be deeply investigated.

In the samples belonging to series M3, the spinel structure was formed from 2 h of milling, being this the only present phase in M3-12. The presence of metallic iron was not detected in any of the M3 samples, indicating the complete consumption of this reagent. Further milling up to 24 h produces in this system the formation of FeOOH as a secondary phase (see Figure 2c).

NaCl was not detected in any of the samples, within the detection limits of XRD, confirming the efficiency of the washing procedure for removing this byproduct after milling.

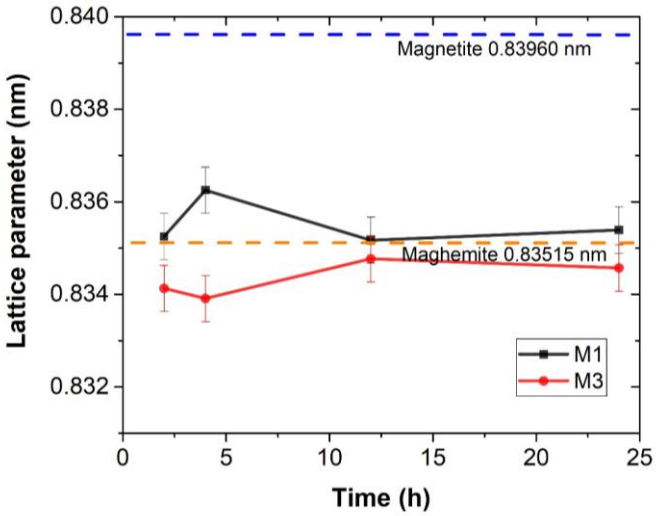


**Figure 3:** Lattice parameter of the spinel phase as a function of milling time for samples M1 (black squares), and M3 (red circles). The theoretical lattice parameters of magnetite and maghemite are indicated with dashed lines.

The calculated lattice parameters in every case are close to values assigned to maghemite, suggesting the formation of this spinel preferably to magnetite as a main magnetic phase of systems M1 and M3 (Figure 3). In both cases, crystallite size values are in the range of 11-14 nm, without showing a clear monotonic tendency with the MC-treatment time.

These results show that the precursor systems M1 and M3 evolve towards the same products because of the availability of metallic iron. In M3, this would occur from the specific addition of metallic iron, and in the series M1 from the gradual wear of the grinding vials and balls. Thus, this reagent seems to be the key to the mechanism of formation of the sought magnetic iron oxides. Iwasaki *et al.* [26-27] reported that iron corrosion of the milling materials played an important role in $Fe_3O_4$ formation, although they demonstrated that this event was small, by measuring the mass loss of the containers and grinding balls. In any case, although both M1 and M3 milled for 12 h produce single-phase spinel, system M3 is the most convenient precursor for the production of iron oxide NPs because of the possibility of controlling the amount of reactive Fe, which is indeed necessary for the reduction of part of the $Fe^{3+}$ ions.

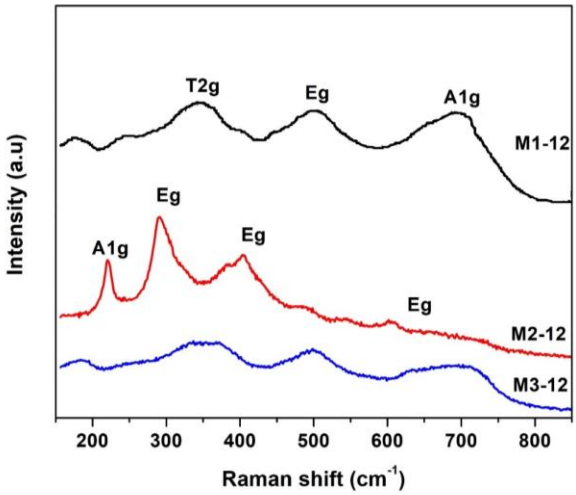


**Figure 4:** Raman spectra of samples M1, M2 and M3, after 12 h of MC-treatment.

Figure 4 shows the Raman spectra of the samples obtained after 12 h of milling the three different precursors. Sample M1-12 shows the three characteristic bands of maghemite at 365, 511 and 700 $cm^{-1}$ [32-37]. A weak band typical of $Fe_3O_4$ could be

masked by the band at 700 $cm^{-1}$ belonging to maghemite. A similar assignment can be made for sample M3-12, although the asymmetry of the band around 650-700 $cm^{-1}$ is noticeable, which might indicate the coexistence of magnetite. On the other hand, sample M2-12 shows the characteristic bands associated to hematite, according to the reported data [32-37]. These results are in good agreement with those obtained by XRD.

Analysis by Raman spectroscopy indicates that systems M1 and M3 react similarly, yielding maghemite. However, we cannot rule out the presence of magnetite. So far, it can be concluded that system M2 is not suitable for the synthesis of ferrimagnetic iron oxide NPs due to the appearance of paramagnetic phases ($\alpha$-$Fe_2O_3$, FeOOH) observed after 12 hours of milling (Figure 2). For this reason, microstructural and magnetic characterization was only performed for samples M1 and M3.

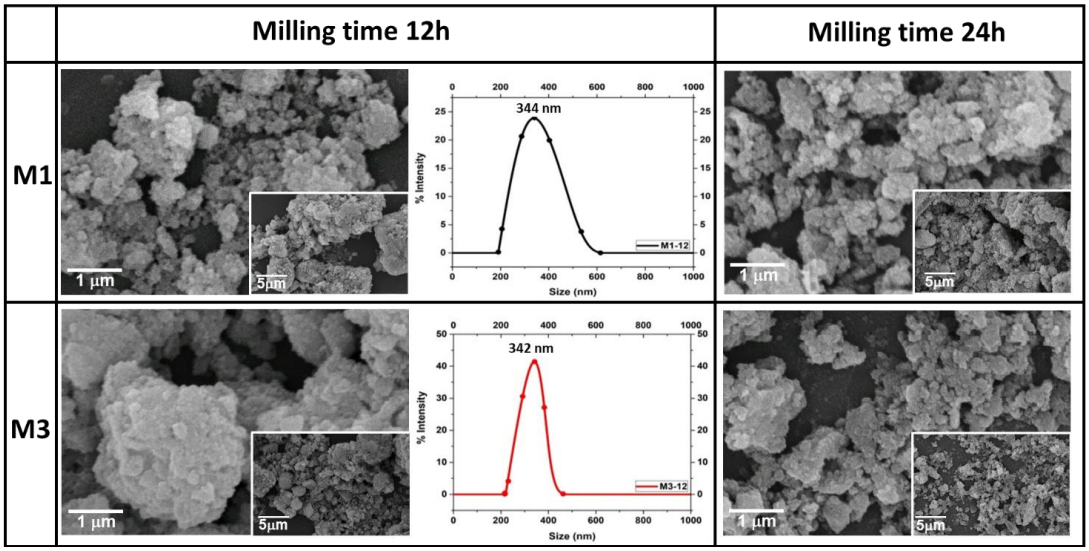


**Figure 5:** SEM images of samples M1 and M3 milled during 12 (left panel) and 24 h (right panel). The insets display images with lower magnification. The central panel shows DLS curves measured for samples M1-12 and M3-12.

In Figure 5, SEM images show the morphological features of the iron oxide NPs obtained from systems M1 and M3, after 12 and 24 h of MC-treatment. Also, the DLS curves of these samples milled for 12 h are displayed in the figure. The images show systems of NPs forming large agglomerates (or clusters) with a wide particle size distribution. The insets allow to estimate the size of agglomerates, ranging from 300-400 nm to a few microns. DLS results indicate that both samples M1-12 and M3-12 have a mean cluster size between 342-344 nm, suggesting that the sonication applied before measurements was successful to disperse micrometric agglomerates into smaller ones. SEM images with higher magnification show particles of nanometric size, although the image resolution is not enough to assess the actual size and shape of single NPs. For this reason, the samples were further analyzed using a transmission electron microscope (TEM).

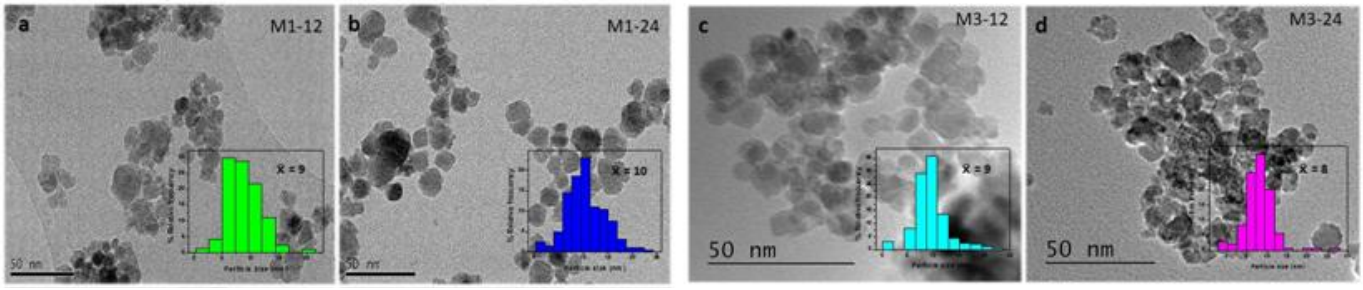


**Figure 6:** TEM images and NP size distributions taken from several images of samples: M1-12 (**a)**, M1-24 (**b)**, M3-12 (**c)** and M3-24 (**d)**.

Figure 6 shows TEM images together with size distributions (measured from several images) of samples M1-12, M1-24, M3-12 and M3-24. The histograms reveal a mean size between 8 and 10 nm for both systems. These values are in good agreement with

the crystallite sizes obtained by the Scherrer formula. It is important to remark here that the sample preparation for TEM observation involves dispersion and separation of the smallest particles of the powders; therefore, TEM images reflect the size of the individual NPs. This outcome, together with SEM and DLS results let infer that the obtained powders are composed of rather round, nanometric particles which form large clusters with mean sizes of about 300 nm, which can be disaggregated with the usual dilution techniques used in TEM sample preparation.

The sphericity of the NPs (or its 2D equivalent, the circularity index) is an important parameter if the final product is to be considered for biomedical applications because the NPs shape influences the flow capacity, bioavailability, and abrasion resistance, among other properties [38]. The calculated circularity values of samples M1-12 and M1-24 are 0.973 and 0.915, respectively. However, in system M3 the values are somewhat lower, being 0.832 and 0.874 for M3-12 and M3-24, respectively. Thus, the obtained NPs from both systems (M1 and M3) have an approximately spherical shape.

Figure 7 shows the room temperature magnetic hysteresis loops of the synthesized iron oxides NPs M1 and M3 for different milling times. All the curves present the typical behavior of soft magnetic materials, characterized by relatively high saturation magnetizations (Ms) and low coercive fields (Hc). All the samples achieve saturation magnetization with the maximum applied field of 20 kOe, which indicates that no superparamagnetic contributions are present in any of the samples.

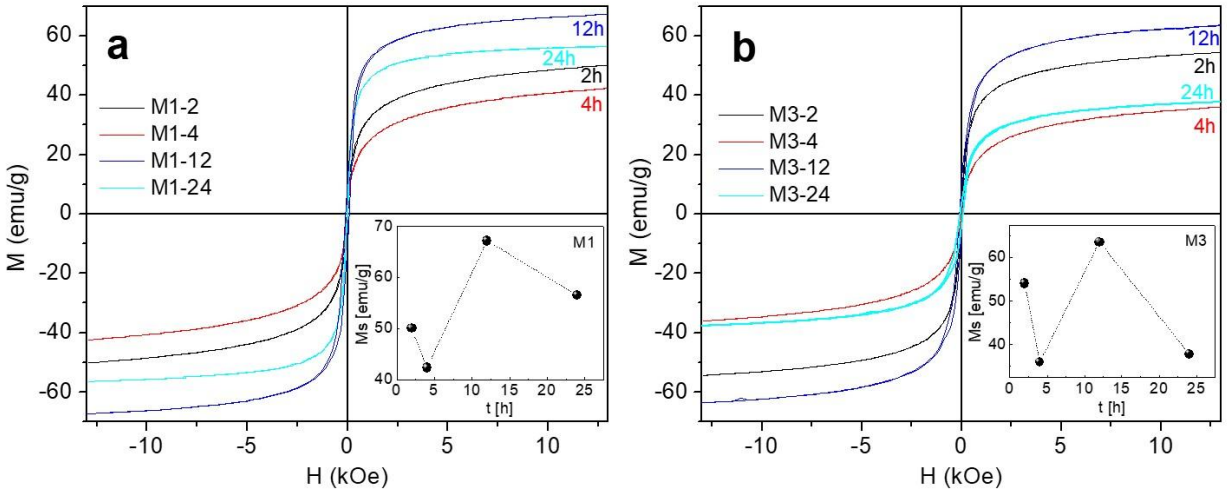


**Figure 7.** Magnetization (M) as a function of applied magnetic field (H) hysteresis loops for samples: M1 **(a)**, and M3 **(b)**, after milling for different times. The insets display the variation of saturation magnetization Ms as a function of milling time, t.

Sample M1-2 is composed of magnetite/maghemite in an unknown proportion. Further milling for two more hours induces changes in the metastable maghemite phase, leading to a lower overall magnetization in M1-4 (see the inset in Figure 7a). This decrease in Ms is overcome after milling for 12 h, obtaining a value of 68.7 emu/g in M1-12. Increasing the milling time up to 24 h generates crystalline damage, and perhaps the formation of secondary phases (not detected by XRD), therefore reducing the total magnetization, as shown in Figure 7a and its inset.

Figure 7b shows the hysteresis loops of samples M3. Just like in the case of series M1, in this system the optimal milling time to obtain the highest Ms is also 12 h. Sample M3-2 decreases its saturation magnetization from 54.1 emu/g to 36 emu/g in M3-4 (Figure 7b and its inset). This important decrease can be attributed to the segregation of FeOOH. MC-treatment up to 12 h produces a saturation magnetization of 65.2 emu/g (Sample M3-12). Further milling results in detriment of the crystalline structure, the appearance of FeOOH as secondary phase and decrease of Ms. For this reason, only M1-12 and M3-12 were further studied to have a deeper insight into their magnetic properties.

Hysteresis loops M(H) were measured at different temperatures from 5 K to 300 K in samples M1-12 and M3-12 and are shown in Figure 8a and 9a, respectively.

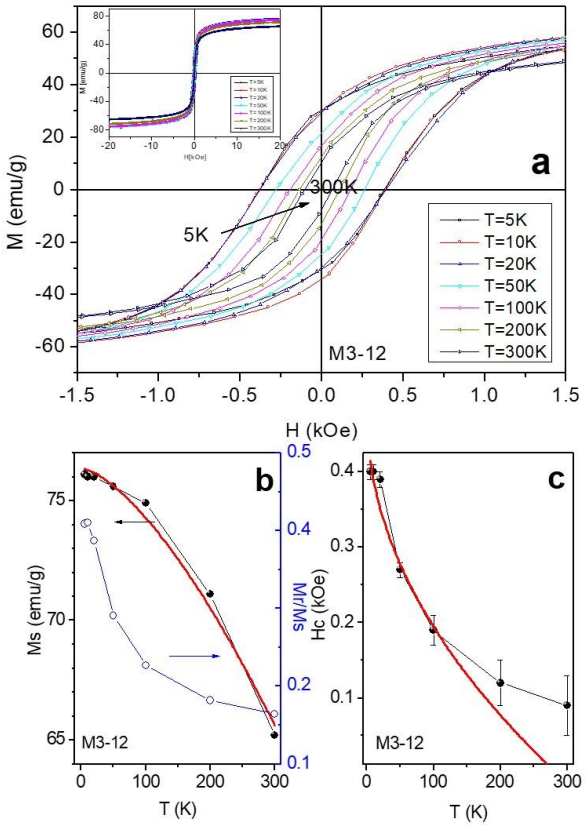


**Figure 8.** Sample M1-12 hysteresis loops measured at different temperatures (a). The inset displays the complete curves in the -20 to 20 kOe field range, while the main figure is a close-up of the low-field region. Saturation magnetization and Mr/Ms (b), and coercivity (c) as a function of temperature are also shown. The red solid line in (b) is the Ms fit using the $T^{3/2}$ Bloch law and the one in (c) corresponds to the $T^{1/2}$ fit for Hc.

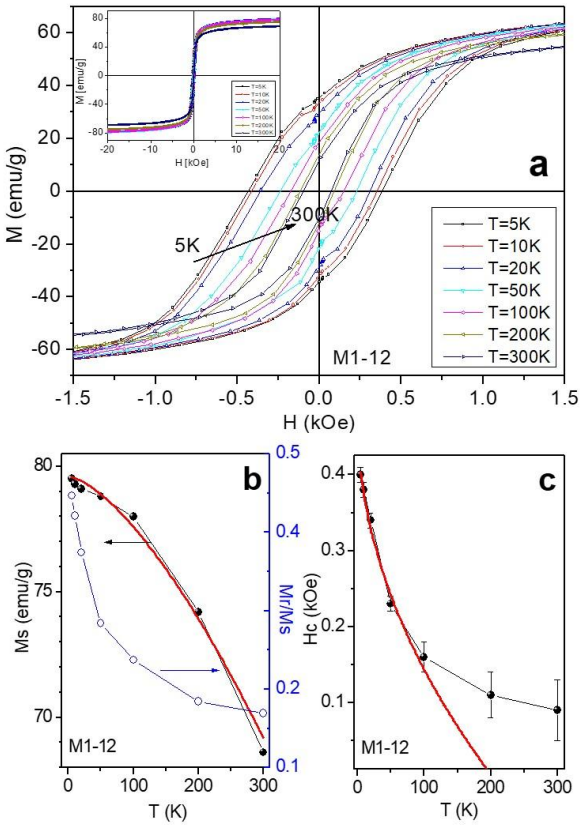


**Figure 9.** Sample M3-12 hysteresis loops measured at different temperatures (a). The inset displays the complete curves in the -20 to 20 kOe field range, while the main figure is a close-up of the low-field region. Saturation magnetization and Mr/Ms (b) and coercivity (c) as a function of temperature are also shown. The red solid line in (b) is the Ms fit using the $T^{3/2}$ Bloch law and the one in (c) corresponds to the $T^{1/2}$ fit for Hc.

Saturation is reached at all temperatures with the maximum applied field of 20 kOe (insets in Figure 8a and 9a), indicating no superparamagnetic contributions in any of the samples. Considering the small mean particle size obtained for both M1-12 and M3-12 by TEM measurements (~9 nm), this result indicates that there is a strong particle interaction. Values of saturation magnetization Ms and squareness (defined as the remanence-to-saturation Mr/Ms ratio) as function of temperature are shown in Figure 8b and 9b. The resemblance in the magnetic behavior of both samples is remarkable, despite somewhat larger saturation magnetization values of sample M1-12 with respect to M3-12. This could be attributed to the shape of the particles, considering that the circularity of sample M3-12 (0.832) is smaller than the one of M1-12 (0.973), as more irregularly-shaped particles may present stray fields and/or surface canting that reduce the net magnetic moment.

As it can be observed in Figure 8b and Figure 9b, Ms decreases steadily with T, being this behavior quite well fitted by the Bloch law $Ms(T)= Ms(0) [1 - B_0 T^{3/2}]$, where Ms(0) is the saturation magnetization at 0K and $B_0$ is a pre-factor. From the fitting, for M1-12 the values Ms(0) and $B_0$ are 79.6 emu/g and 2.5 x $10^{-5}$ $K^{-3/2}$, respectively, and for M3-12, 76.4 emu/g and 2.7 x $10^{-5}$ $K^{-3/2}$, respectively. These results are in agreement with the same $T^{3/2}$ dependence observed by Martínez *et al.* for maghemite NPs, with a prefactor $B_0$=2.8 x $10^{-5}$ $K^{-3/2}$ [39] and indicate the presence of spin-wave excitations up to room temperature.

The squareness Mr/Ms values of both samples are similar and well below the expected 0.5 value for uniaxial, non-interacting particles with random orientation, indicating strong particles interactions at all temperatures, as shown in Figure 8b and Figure 9b. (right axis).

The behavior of coercivity as a function of temperature is plotted in Figures 8c and 9c for M1-12 and M3-12, respectively. The data were fitted with the expression derived originally by Bean and Livingston for an assembly of non-interacting single-domain particles of volume V [40] $Hc(T)=Hc(0)\,[1-(T/T_0)^{1/2}]$, where Hc(0) is the coercive field at T=0 K and $T_0$ is the blocking temperature if the particles are in the blocked state. This expression is a simplified model of the particles moment's thermal activation over an anisotropy barrier but is usually used to describe more complex systems by considering effective contributions.

The fitting is quite good at temperatures below 100 K, but interaction and size effects become important at higher T and the simplistic model of thermal activation fails to describe the experimental data in both samples at temperatures above 100 K. This discrepancy has been usually observed in real systems, and it is attributed to the particles size distribution [41], since the larger particles reverse their magnetization through a nucleation-and-propagation process, therefore are not well described by the model. It is interesting to note that the fittings give Hc(0)=47.8 mT for both samples but differ in the critical temperature, being $T_0$ =215 K for M1-12 and $T_0$ =285 K for M3-12. Considering that $T_0$=K V/(25 $k_B$), where K is the magnetic anisotropy constant (4.6 kJ/$m^3$ for maghemite [42] and $k_B$ is Boltzmann constant), a mean effective diameter can be estimated for spherical particles, giving 46 nm for M1-12 and 52 nm for M3-12. These values are of the same order of magnitude than the exchange length Lex=46.6 nm reported for maghemite [42] and indicate that inter-particles ferrimagnetic interactions are expected in both samples.

Ms, Mr/Ms and Hc values for both M1-12 and M3-12 agree with other reports for magnetite and maghemite similar particles making it very difficult to univocally determine the actual phase from these values alone [2, 43- 46].

Magnetization versus temperature M(T) curves were measured between 4 and 300 K following the zero field cooling-field cooling (ZFC-FC) protocol and the corresponding curves are shown in Figure 10a and 10b for samples M1-12 and M3-12, respectively. In ZFC mode, the sample is cooled from room temperature down to 4 K with no applied field. A magnetic field of 100 Oe is turned on at 4 K and the values M(T) are registered while warming up the system up to 300 K. For the FC curve, the process is repeated while keeping the applied field on, while cooling from 300 K to 4 K. The M(T) values in FC mode are also recorded in warming.

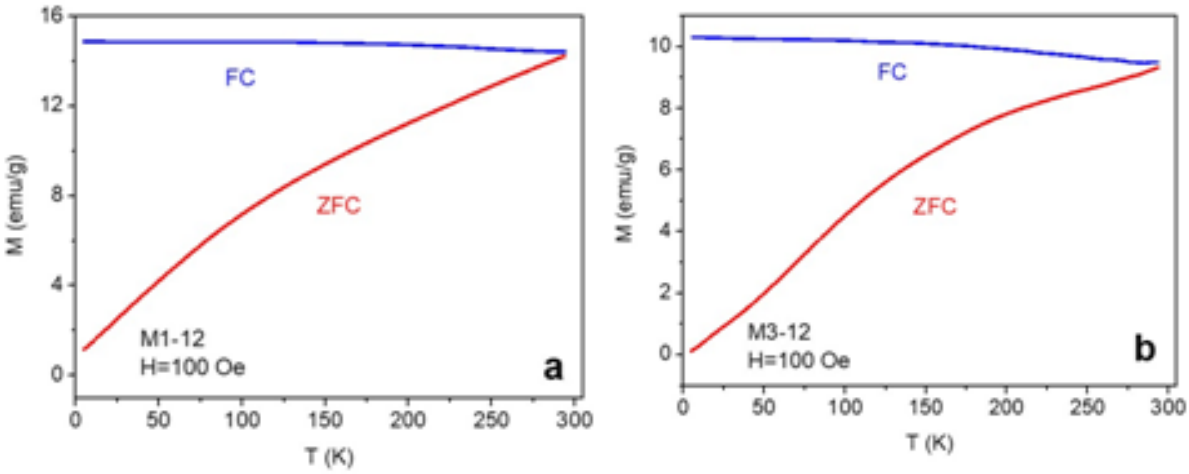


**Figure 10.** Zero field cooling - Field cooling curves of samples M1-12 (a) and M3-12 (b).

The absence of the Verwey transition in both samples is clear from the measurements since a steady increase of M with T is observed in the whole temperature range, and may indicate that the samples are mainly composed of maghemite [47]. However, the presence of small amounts of magnetite cannot be completely ruled out, since it has been reported that the Verwey transition can be suppressed in particles smaller than 20 nm [46]. The ZFC and FC curves do not overlap in the whole temperature range, indicating strong particles interaction in both samples and irreversible temperatures above 300 K, in agreement with the previous discussion on magnetic results.

**CONCLUSIONS**

Iron oxide NPs with magnetization values larger than 65 emu/g were synthesized by MC-treatment performed in stainless steel vials in air atmosphere. It was determined that 12 h of MC-treatment was the optimal time to obtain magnetic NPs and to avoid their subsequent deterioration. The simplicity and efficiency of the method allows obtaining mostly maghemite NPs with mean

crystallite size between 11 and 14 nm, with a rather spherical shape. Among the three reactive systems studied in this work, those involving metallic Fe (either by addition or by wear of the vials), produced materials with the best magnetic properties.

According to the composition of each system, the following conclusions can be summarized:

- The mixture of $FeCl_3.6H_2O$ and NaOH with molar ratio 2:6 (M1) allowed to obtain magnetic NPs after 12 hours of MC-treatment with good stability, without segregation of secondary phases. The reactivity of this system is associated to the metallic Fe that comes from the milling vials and balls, which is detrimental for the compositional control. This system produced clusters of about 300 nm, formed by NPs with a mean size of ≈ 9 nm with high values of saturation magnetization (Ms=68.7 emu/g).

- The mixture of $FeCl_2.4H_2O$, $FeCl_3$ $.6H_2O$ and NaOH with molar ratio 1:2:8 (M2) generated a low proportion of magnetic phases at short treatment times, and a high proportion of secondary phases at longer milling times. The system M2 is not considered a suitable reactive mixture for obtaining single-phase magnetic NPs.

- The mixture of $FeCl_3$ $.6H_2O$, Fe and NaOH with molar ratio 8:1:24 (M3) showed to be suitable for obtaining magnetic NPs, after 12 h of MC-treatment. These conditions led to obtain clusters of ≈ 300 nm, formed by NPs with a mean size of ≈ 9 nm and high saturation magnetization (Ms=65.2 emu/g).

All the collected evidence allows to conclude that reactive mixture M3 mechanochemically treated for 12 h is the most convenient route to obtain iron oxide NPs, with a controlled composition and excellent magnetic properties. Selective centrifugation could be an interesting additional tool in order to obtain a narrower size distribution of these NPs. Finally, greater effort must be devoted to improving the dispersion of the produced magnetic NPs, which could be achieved starting from diluted reactive systems, by addition of NaCl as a solid diluent.

**ACKNOWLEDGEMENTS**

The authors gratefully thank CONICET, FONCyT, Universidad Nacional de Córdoba and Universidad Nacional de Mar del Plata for the financial support given to this work.

**REFERENCES**

1. U. Enz, Magnetism and Magnetic Materials: Historical Developments and Present Role in Industry and Technology. Handbook of Magnetic Materials, Vol. 3. North-Holland, 1982.
2. U.S.R.M Cornell, The Iron Oxides: Structure, Properties, Occurrences and Uses, Wiley-VCH Weinheim, 2003.
3. M. Sugimoto, The Past, Present, and Future of Ferrites. J. Am. Ceram. Soc., 82 (1999) 269–80.
4. J. Smit, H. P. J. Wijn, Ferrites, Philips Technical Library, Eindhoven, The Netherlands, 1959.
5. N.A. Spaldin, Magnetic Materials: Fundamentals and Applications, 2nd Edition, Cambridge University Press, Cambridge, 2011.
6. D. Ramimoghadam, S. Bagheri, S. B. A. Hamid, Progress in electrochemical synthesis of magnetic iron, J of Magnetism and Magnetic Materials, 368 (2014): 207-229.
7. S. M. Dadfar, K. Roemhild, N. I. Drude, S. Von Stillfried, R. Knüchel, F. Kiessling, T. Lammers, Iron oxide nanoparticles: Diagnostic, therapeutic and theranostic applications. Advanced Drug Delivery Reviews, 2019: 302-325.
8. J. W.M. Bulte, Superparamagnetic iron oxides as MPI tracers: A primer and review of early applications. Advanced Drug Delivery Reviews, 2019: 293-301.
9. A. G. Roca, L. Gutiérrez, H. Gavilán, M. E. Fortes B, S. Veintemillas-V, M. del Puerto M, Design strategies for shape-controlled magnetic iron oxide nanoparticles. Advanced Drug Delivery Reviews, 2019: 68-104.
10. C. Song, W. Sun, Y. Xiao, X. Shi. Ultrasmall iron oxide nanoparticles: synthesis, surface modification, assembly, and biomedical applications, Drug Discovery Today, 2019: 835-844.
11. T. A. Lastovina, A. P. Budnyk, S.P. Kubrin, A. V. Soldatov, Microwave-assisted synthesis of ultra-small iron oxide nanoparticles for biomedicine. Mendeleev Communications, 2018: 167-169.
12. A. Hassanjani-Roshan, M. Reza V, A. Shokuhfar, Z. Rajabali, Synthesis of iron oxide nanoparticles via sonochemical method and their characterization, Particuology, 2011: 95-99.
13. K. Petcharoen, A. Sirivat. Synthesis and characterization of magnetite nanoparticles via the chemical co-precipitation method, Materials Science and Engineering B, 2012: 421-427.
14. L. Shen, Y. Qiao, Y. Guo, S. Meng, G. Yang, M. Wu, J. Zhao, Facile co-precipitation synthesis of shape-controlled magnetite nanoparticles, Ceramics International, 2014: 1519-1524.
15. K. Sathya, R. Saravanathamizhana, G. Baskar, Ultrasound assisted phytosynthesis of iron oxide nanoparticle, Ultrasonics - Sonochemistry, 2017: 446-451.
16. A. Lassoued, M. Saber L, B. Dkhil, S. Ammar, A. Gadri, Synthesis, photoluminescence and Magnetic properties of iron oxide ($\alpha$-$Fe_2O_3$) nanoparticles through precipitation or hydrothermal methods, Physica E: Low-dimensional Systems and Nanostructures, 2018: 212-219.
17. P. Bhavani, C.H. Rajababu, M.D. Arif, I. V. Subba R, N. Ramamanohar R, Synthesis of high saturation magnetic iron oxide nanomaterials via low temperature hydrothermal method. J. of Magnetism and Magnetic Materials, 2017: 459-466.

18. P.G. McCormick, T. Tsuzuki, J.S. Robinson, J. Ding, Nanopowders Synthesized by Mechanochemical Processing, Adv. Mater. 13 (2001) 1008–1010.
19. T. Tsuzuki, P.G. McCormick, Mechanochemical synthesis of nanoparticles, J. Mater. Sci. 39 (2004) 5143 – 5146.
20. T. Tsuzuki, F. Schäffel, M. Muroi, P.G. McCormick, Magnetic properties of mechanochemically synthesized γ-$Fe_2O_3$ nanoparticles, J. Alloys Compd. 509 (2011) 5420–5425.
21. A.A. Cristóbal, P.M. Botta, Mechanochemically assisted synthesis of nanocrystalline $BiFeO_3$. Mater. Chem. Phys. 139 (2013) 931 - 935.
22. J.A. Castrillón Arango, A.A. Cristóbal, C.P Ramos, P.G. Bercoff, P.M. Botta, Mechanochemical synthesis and characterization of nanocrystalline $Ni_{1-x}Co_xFe_2O_4$ ($0 \leq x \leq 1$) ferrites. J. Alloys Compd. 811 (2019) 152044.
23. S. S. Staniland, A. Rawlings, J. Bramble, J. Tolosa, O. Wilson, J. C. García M, C. Binns. Novel Methods for the Synthesis of Magnetic Nanoparticles, Frontiers of Nanoscience, Elsevier, 85-128. Amsterdam, The Netherlands: Chris Binns, 2014.
24. B. Medina, M. G. Verdério F, J. Martins G, F. Maesta B, F. A. Pereira S, M. Pereira M, A. Bail, R. Block S, Solventless preparation of $Fe_3O_4$ and $Co_3O_4$ nanoparticles: A mechanochemical approach, Materials Chemistry and Physics , 2019: 318-322.
25. Jae-Wan Park, Cheol-Min Park, $Fe_3O_4$ nanoparticles produced by mechanochemical transformation: A highly reversible electrode material for Li-ion batteries, Materials letters , 2017: 131-134.
26. T. Iwasaki, N. Sato, K. Kosaka, S.Watano, T. Yanagida, T. Kawai, Direct transformation from goethite to magnetite nanoparticles by mechanochemical reduction, Journal of Alloys and Compounds, 2011: L34-L37.
27. T. Iwasaki, N. Sato, H. Nakamura, S. Watano, An experimental investigation of aqueous-phase synthesis of magnetite nanoparticles via mechanochemical reduction of goethite, Advanced Powder Technology, 2013: 482-486.
28. J.F. de Carvalho, S.N. de Medeiros, M.A. Morales, A.L. Dantas, A.S. Carrico, Synthesis of magnetite nanoparticles by high energy ball milling, Applied Surface Science, 2013: 84-87.
29. B.D. Cullity, S.R. Stock, Elements of X-ray Diffraction, third ed., Prentice-Hall Inc., New Jersey, 2001.
30. S.L. James, C.J. Adams, C. Bolm, D. Braga, P. Collier et al., Mechanochemistry: opportunities for new and cleaner synthesis, Chem. Soc. Rev., 41 8 (2012) 413–447.
31. L. Takacs, The historical development of mechanochemistry, Chem. Soc. Rev. 42 (2013) 7649–7659.
32. C. Markovski, J.M. Byrne, E. Lalla, A.D. Lozano-Gorrín, G. Klingelhöfer, F. Rull, A. Kappler, T. Hoffmann, C. Schröder, Abiotic versus biotic iron mineral transformation studied by a miniaturized backscattering Mössbauer spectrometer (MIMOS II), X-ray diffraction and Raman spectroscopy, Icarus, 296 (2017): 49-58.
33. C.J. Letti, L.G. Paterno, M.A. Pereira-da-Silva, P.C. Morais, M.A.G. Soler, The role of polymer films on the oxidation of magnetite nanoparticles, Journal of Solid State Chemistry, 246 (2017): 57-64.
34. I. Martínez M, C. Gutiérrez W, C. Argánis J, A. R. Vilchis N, Reduction of maghemite to magnetite over 304SS, in the presence of silver nanoparticles, Surface & Coatings Technology, 324 (2017): 338-344.
35. L. Slavov, M.V.Abrashev, T. Merodiiska, Ch. Gelev, R. E. Vandenberghe, I. Markova-Deneva, I. Nedkov, Raman spectroscopy investigation of magnetite nanoparticles in ferrofluids, Journal of Magnetism and Magnetic Materials, 322 (2010): 1904-1911.
36. M.Krajewski, K. Brzozka, M. Tokarczyk, G. Kowalski, S. Lewinska, A. Slawska-Waniewska, W. Syuan Lin , H. Ming Lin, Impact of thermal oxidation on chemical composition and magnetic properties of iron nanoparticles, Journal of Magnetism and Magnetic Materials, 458 (2018): 346-354.
37. M. Bajt Leban, T. Kosec, Characterization of corrosion products formed on mild steel in deoxygenated water by Raman spectroscopy and energy dispersive X-ray spectrometry, Engineering Failure Analysis, 79 (2017): 940-950.
38. L. Kopanja, D. Žunić, B. Lončar, S. Gyergyek, M. Tadić, Quantifying shapes of nanoparticles using modified circularity and ellipticity measures, Measurement, 92 (2016) 252-263.
39. B. Martínez, A. Roig, X. Obradors, E. Molins, A. Rouanet, and C. Monty, Magnetic properties of γ-$Fe_2O_3$ nanoparticles obtained by vaporization condensation in a solar furnace. J. Appl. Phys. **79**(1996), 2580
40. C. P. Bean and J. D. Livingston. Superparamagnetism. J. Appl Phys. 30, 4 (1959) S120-S129
41. M. Knobel, W. C. Nunes, L. M. Socolovsky, E. De Biasi, J. M. Vargas, J. C. Denardin, Superparamagnetism and other magnetic features in granular materials: a review on ideal and real systems J. Nanosci. Nanotechnol. 8 (2008) 2836-2857.
42. Hou, X. F. Nie, H. L. Luo, Studies on the magnetic viscosity and the magnetic anisotropy of γ-$Fe_2O_3$ powders. D. L. Appl. Phys. A 66 (1998) 109–114
43. H. Itoh and T. Sugimoto, Systematic control of size, shape, structure, and magnetic properties of uniform magnetite and maghemite particles. Journal of Colloid and Interface Science 265 (2003) 283–295.
44. D. J. Dunlop, Coercive forces and coercivity spectra of submicron magnetites. Earth and Planetary Science Letters. 78, (1986) 288-295.
45. C.J. Goss, Saturation Magnetisation, Coercivity and Lattice Parameter Changes in the System $Fe_3O_4$-$Fe_2O_3$, and Their Relationship to Structure. Phys Chem Minerals (1988) 16:164-171.
46. G. F. Goya, T. S. Berquó, F. C. Fonseca, and M. P. Morales, Static and dynamic magnetic properties of spherical magnetite nanoparticles. J. Appl. Phys. 94, (2003) 3520.
47. Özden Özdemir and David J. Dunlop, The effect of oxidation on the Verwey transition in magnetite. Geophysical Research Letters, Vol. 20, No. 16 (1993) 1671-1674.